Title

Cellular mechanisms for response heterogeneity among L2/3 pyramidal cells in whisker somatosensory cortex

Journal

Journal of Neurophysiology, 112(2)

ISSN

0022-3077

Authors

Elstrott, Justin
Clancy, Kelly B
Jafri, Haani
et al.

Publication Date

2014-07-15

DOI

10.1152/jn.00848.2013

Peer reviewed

Cellular mechanisms for response heterogeneity among L2/3 pyramidal cells in whisker somatosensory cortex

Justin Elstrott, Kelly B. Clancy, Haani Jafri, Igor Akimenko and Daniel E. Feldman

J Neurophysiol 112:233-248, 2014. First published 16 April 2014; doi:10.1152/jn.00848.2013

Journal of Neurophysiology publishes original articles on the function of the nervous system. It is published 12 times a year (monthly) by the American Physiological Society, 9650 Rockville Pike, Bethesda MD 20814-3991. ISSN: 0022-3077, ESSN: 1522-1598. Visit our website at http://www.the-aps.org/.

J Neurophysiol 112: 233–248, 2014.
First published April 16, 2014; doi:10.1152/jn.00848.2013.

Cellular mechanisms for response heterogeneity among L2/3 pyramidal cells in whisker somatosensory cortex

Justin Elstrott,[1] Kelly B. Clancy,[2] Haani Jafri,[1] Igor Akimenko,[1] and Daniel E. Feldman[1]
[1]*Department of Molecular and Cellular Biology and Helen Wills Neuroscience Institute, University of California, Berkeley, California; and* [2]*Biophysics PhD Program, University of California, Berkeley, California*

Submitted 30 November 2013; accepted in final form 9 April 2014

Elstrott J, Clancy KB, Jafri H, Akimenko I, Feldman DE. Cellular mechanisms for response heterogeneity among L2/3 pyramidal cells in whisker somatosensory cortex. *J Neurophysiol* 112: 233–248, 2014. First published April 16, 2014; doi:10.1152/jn.00848.2013.—Whisker deflection evokes sparse, low-probability spiking among L2/3 pyramidal cells in rodent somatosensory cortex (S1), with spiking distributed nonuniformly between more and less responsive cells. The cellular and local circuit factors that determine whisker responsiveness across neurons are unclear. To identify these factors, we used two-photon calcium imaging and loose-seal recording to identify more and less responsive L2/3 neurons in S1 slices in vitro, during feedforward recruitment of the L2/3 network by L4 stimulation. We observed a broad gradient of spike recruitment thresholds within local L2/3 populations, with low- and high-threshold cells intermixed. This recruitment gradient was significantly correlated across different L4 stimulation sites, and between L4-evoked and whisker-evoked responses in vivo, indicating that a substantial component of responsiveness is independent of tuning to specific feedforward inputs. Low- and high-threshold L2/3 pyramidal cells differed in L4-evoked excitatory synaptic conductance and intrinsic excitability, including spike threshold and the likelihood of doublet spike bursts. A gradient of intrinsic excitability was observed across neurons. Cells that spiked most readily to L4 stimulation received the most synaptic excitation but had the lowest intrinsic excitability. Low- and high-threshold cells did not differ in dendritic morphology, passive membrane properties, or L4-evoked inhibitory conductance. Thus multiple gradients of physiological properties exist across L2/3 pyramidal cells, with excitatory synaptic input strength best predicting overall spiking responsiveness during network recruitment.

cortex; map plasticity; synaptic mechanisms; somatosensory; vibrissa

NEURONS in L2/3 of rodent somatosensory (S1) cortex encode whisker stimuli with relatively few action potentials, an example of sparse coding (Barlow 1972; Olshausen and Field 2004; Wolfe et al. 2010). Sparse coding reflects both neural tuning to specific whisker stimuli and low average firing probability even when empirically determined optimal stimuli are presented (Crochet et al. 2011; de Kock et al. 2007; Jadhav et al. 2009). Sparse activity is organized nonuniformly across the L2/3 neuron population, with just ~10% of neurons generating the majority of whisker-evoked spikes and most neurons having low response probability (Crochet et al. 2011; de Kock et al. 2007; O'Connor et al. 2010a). L2/3 firing is sparser than most other layers (de Kock et al. 2007; O'Connor et al. 2010b).

What cellular and circuit mechanisms underlie the heterogeneity of response probability among L2/3 neurons? Among pyramidal cells, low- and high-responsive neurons may represent two distinct cell classes, extremes of a response gradient, or neurons with homogeneous cellular properties but different sensory tuning (Barth and Poulet 2012). Responsiveness may map onto distinct morphological classes of L2/3 pyramidal cells (Oberlaender et al. 2012). More responsive neurons have more depolarized synaptic reversal potentials to whisker input in vivo, suggesting that they receive greater excitation and/or less inhibition (Crochet et al. 2011). More spontaneously active L2/3 pyramidal cells, identified by expression of the activity-dependent label fosGFP, receive more local excitation and form a preferentially interconnected synaptic network, but whether these are the more whisker-responsive neurons is unknown (Benedetti et al. 2013; Yassin et al. 2010). An unbiased search to define populations of more and less responsive pyramidal cells, and to identify additional cellular factors that distinguish them, remains lacking.

To efficiently identify more and less responsive pyramidal cells during feedforward network activation, we used two-photon calcium imaging in S1 slices to measure the ability of L4 extracellular stimulation to elicit action potentials in L2/3 neurons within a small imaging field. L4 stimulation primarily activates a mixture of L4 and L5a feedforward excitatory inputs to L2/3, as well as feedforward and monosynaptic inhibition (Shepherd et al. 2005; Shepherd and Svoboda 2005). This "mixed feedforward input" both directly evokes spikes in some L2/3 neurons and recruits recurrent L2/3 excitation and inhibition that further shape spiking recruitment of the network. Our goal was to test for more responsive and less responsive cell classes by identifying cellular and circuit properties that predict spiking responsiveness during this complex network recruitment. We also tested whether neurons that were more responsive to L4 stimulation were also more responsive to natural sensory stimulation in vivo.

In slices, we observed a gradient of spike recruitment across L2/3 pyramidal cells in which low-threshold (more responsive) and high-threshold (less responsive) neurons were spatially intermixed. This response gradient was correlated across different L4 stimulation sites, indicating that a component of responsiveness is independent of tuning to specific feedforward inputs. In whole cell recordings, low-threshold pyramidal cells received more L4-evoked excitatory synaptic conductance and were less intrinsically excitable, including higher spike threshold, weaker firing rate-current (*F-I*) curve, and lower tendency to generate initial doublet spike bursts. Overall, a gradient of intrinsic excitability was found across L2/3 pyramidal cells, which opposed the gradient of L4-evoked spiking responsiveness. Thus multiple cellular and local circuit properties vary among L2/3 pyramidal neurons that correlate with the gradient

Address for reprint requests and other correspondence: D. E. Feldman, Dept. of Molecular and Cell Biology, 142 LSA #3200, UC Berkeley, Berkeley CA 94720 (e-mail: dfeldman@berkeley.edu).

of responsiveness during feedforward network recruitment. In vivo, L4-evoked and whisker-evoked response gradients were correlated, suggesting that the cellular factors that contribute to feedforward network recruitment are also important determinants of whisker responsiveness among L2/3 neurons.

MATERIALS AND METHODS

All procedures were approved by the UC Berkeley Institutional Animal Care and Use Committees and are in accordance with National Institutes of Health guidelines. Slice physiology experiments used Long-Evans rats. In vivo experiments used C57BL/6 mice.

Slice physiology. Acute slices of S1 cortex (400 μm) were prepared from P18–P24 rats in the parasagittal, "across-row" plane that allows identification of specific whisker barrels (House et al. 2011). Slices were cut in chilled low-sodium, low-calcium solution [in mM: 85 NaCl, 75 sucrose, 25 D-(+)-glucose, 4 $MgSO_4$, 2.5 KCl, 1.25 $Na_2HPO_4 \cdot H_2O$, 0.5 ascorbic acid, 25 $NaHCO_3$, 0.5 $CaCl_2$], then transferred to normal Ringer solution [in mM: 119 NaCl, 26.2 $NaHCO_3$, 11 D-(+)-glucose, 1.3 $MgSO_4$, 2.5 KCl, 1 NaH_2PO_4, 2.5 $CaCl_2$, bubbled with 95% O_2-5% CO_2, pH 7.30, 310 mosM], and then incubated for 30 min at 30°C and 1–6 h at room temperature before recording. S1 was identified from the characteristic barrel pattern visualized by transillumination (Agmon and Connors 1991).

All recordings were made at 30°C with 2.5- to 4-MΩ pipettes and Multiclamp 700A or 700B amplifiers (Molecular Devices, Sunnyvale, CA). L4 was stimulated with a bipolar stimulating electrode (115-μm tip separation, FHC, Bowdoin, ME) in the center of a L4 barrel. Imaging and recording were performed in the region of L2/3 located midway between the pia and the top of L4, in the stimulated barrel column. L4-evoked field potentials were measured in the center of the L2/3 recording field, with 2-MΩ electrodes filled with Ca^{2+}-free Ringer solution. Each field potential waveform was the average of three traces.

Two-photon calcium imaging in slice. Population calcium imaging was performed in L2/3 with Oregon Green BAPTA-1 AM (OGB-1 AM, Molecular Probes), which was bolus loaded into L2/3 cells (Stosiek et al. 2003). Fifty micrograms of OGB-1 AM was dissolved into 5 μl of DMSO containing 20% pluronic acid (TEFLabs). Forty-five microliters of a buffer solution (in mM: 150 NaCl, 2.5 KCl, 10 HEPES, 290–300 mosM, pH 7.3) was then added to give a final OGB-1 AM concentration of 0.8 mM. The solution was applied via a 3-MΩ pipette in L2/3 (8 psi, 1 min). Slices were maintained on the rig at 30°C for >30 min prior to imaging.

Two-photon images were acquired at 3.9 Hz on a modified Olympus BX-51 microscope equipped with a tunable femtosecond Ti:sapphire laser (Chameleon, Coherent) (Wei et al. 2010). Excitation wavelength was 800 nm, and emission was at 525 nm (500- to 550-nm band pass, Chroma). Imaging was performed through a ×60 Olympus Fluoplan objective (0.9–1.0 NA), using Fluoview software to scan a 512 × 512 pixel area (128 × 128 μm). The point spread function was ~0.5 μm in XY and 2.5 μm in Z. XYT movies were corrected for drift in the image plane by aligning to the mean image with ImageJ (Abràmoff et al. 2004) with the StackReg plug-in (Thévenaz et al. 1998) and were denoised with a 3-pixel median filter in *x*, *y*, and *t*. Regions of interest (ROIs) were manually drawn around somata. Cells with saturated somatic fluorescence, indicative of glial cells or damaged neurons, were excluded (Stosiek et al. 2003).

To measure L4-evoked spiking in the L2/3 neuron population, L4 was stimulated via an extracellular electrode (200-μs duration, 0.125-Hz rate, 10 stimuli per intensity). The fluorescence trace for each L2/3 neuron was calculated as

$$\Delta F/F = (F_i - F_{base})/F_{base}$$

where F_i is the mean ROI fluorescence in the *i*th frame and F_{base} is mean ROI fluorescence in the 3.5 s prior to onset of the L4 stimulus train. There were essentially no spontaneous calcium transients in the baseline period. Decay kinetics in neuronal ROIs were slower than in neuropil regions in each imaging field. Spike-related calcium transients were detected with a nonnegative deconvolution algorithm (Vogelstein et al. 2010) on the ΔF/F trace of each cell, yielding an arbitrary value of spike probability for each frame. This spike probability was thresholded at 0.15, resulting in a binary event train for each cell. This threshold value was determined from loose-seal calibration experiments (see RESULTS). To minimize false positives in nonspiking cells, we also applied a minimum signal-to-noise ratio (SNR) for calcium event magnitude (Sasaki et al. 2008):

$$SNR = \text{median}(\text{event amplitude})/\text{std}(F_{base})$$

where the numerator is the median peak ΔF/F for all identified spiking responses. Cells with SNR < 3 were considered nonspiking (as verified by loose-seal recordings). For each L4 stimulus, a spiking response was defined as the occurrence of an event (a suprathreshold calcium transient) in the frame immediately following L4 stimulation, which represents the interval 0–250 ms after stimulus.

To measure L4-evoked spike thresholds, the probability of spiking, *P*(spike), was calculated from the 10 trials at each stimulation intensity. L4-evoked activation threshold was calculated as the stimulus intensity that yielded *P*(spike) = 0.50, either from a sigmoid fit across stimulation intensity or by interpolating the *P*(spike) values. To allow comparison of L4-evoked responses across slices, stimulation intensity was measured not as absolute stimulation current but as the peak negative amplitude of the L4-evoked field potential measured in the center of the L2/3 imaging field, normalized to the maximal field potential amplitude observed in that column (see Fig. 2*A*, *inset*). This measure reflects the average L4-evoked synaptic drive across many or all neurons in the imaging field. For comparison of rank order of L4-evoked recruitment of cells, ties were assigned the average rank of the two (or more) tied cells. Analysis was performed with custom routines in MATLAB.

Synaptic conductance measurement. Whole cell voltage-clamp recordings were targeted to high- and low-responsive cells after calcium imaging, using Cs gluconate internal solution (in mM: 108 D-gluconic acid, 108 CsOH, 20 HEPES, 5 tetraethylammonium-Cl, 2.8 NaCl, 0.4 EGTA, 4 MgATP, 0.3 NaGTP, 5 BAPTA, 5 QX314 bromide, pH 7.2, 295 mosM). Series resistance (R_{series}) was compensated 80%. Pyramidal cells were excluded if membrane potential (V_m) at break-in was > −60 mV, R_{series} > 15 MΩ (uncorrected), or input resistance (R_{input}) < 100 MΩ. V_m values for voltage-clamp recordings were corrected for the measured liquid junction potential (10–12 mV). Data acquisition and analysis used custom software in Clampex (Molecular Devices), IGOR Pro (WaveMetrics, Portland, OR), and MATLAB (MathWorks). L4-evoked excitatory and inhibitory synaptic conductances were calculated from currents recorded at four holding potentials (V_{hold}; −90, −68, −40, and 0 mV), as previously described (House et al. 2011).

Intrinsic excitability. Intrinsic excitability measurements were made in whole cell current clamp, using K gluconate internal solution (in mM: 116 K gluconate, 20 HEPES, 6 KCl, 2 NaCl, 0.5 EGTA, 4 MgATP, 0.3 NaGTP, 5 Na_2 phosphocreatine, pH 7.2, 295 mosM). For these experiments, L4-evoked response threshold was determined from loose-seal recordings (Perkins 2006) rather than calcium imaging. Loose-seal recording was made in voltage-clamp configuration with K gluconate internal solution, with recording beginning >2 min after a sub-GΩ seal was established, to allow recovery of network excitability. V_{hold} was carefully adjusted to maintain 0 pA holding current, which was critical to avoid biasing the spike probability. The L4-evoked activation threshold was defined as the L4 stimulation intensity (normalized to the peak maximal field potential) required to drive spiking in 50% of trials.

Resting V_m was measured immediately after break-in. Passive and active intrinsic properties were determined with 500-ms current injections (−400 pA to 700 pA), using 1-s sweep intervals. R_{input} was

defined as the slope of the linear fit to steps in the interval of −50 pA to 50 pA. Membrane capacitance (C_m) was determined with a double exponential fit to the first 100 ms of a −50-pA step (Golowasch et al. 2009). I_h was estimated from V_m sag ratio during a −200-pA current injection step, sag defined as

$$\text{sag ratio} = (V_{SS} - V_{base})/(V_{min} - V_{base})$$

where V_{ss} is the mean steady-state V_m at the end of the current step, V_{base} is the mean voltage preceding step onset, and V_{min} is the minimum V_m 120–140 ms after step onset; 120–140 ms was chosen to avoid contamination by a transient potassium conductance observed with strong hyperpolarization at step onset. Medium afterhyperpolarization (mAHP) was defined as the minimum *V*m in the 100 ms following a spike elicited with a 2-ms, 600–1,200 pA depolarizing current step, averaged over 5 trials. The passive components were removed by subtracting the mean waveform to a hyperpolarizing step of the same size. *V*m was held near −50 mV with DC current injection during mAHP measurement. Spiking was characterized by 500-ms positive current injection from resting potential (V_{rest}), with spike threshold defined as the time point when the second derivative of V_m exceeded 6 standard deviations above baseline. Initial spike doublets were defined as spikes with interspike interval (ISI) < 10 ms. Burst step was defined at the current amplitude (above rheobase) required to elicit an initial spike doublet. R_{series} was compensated by bridge balance. The liquid junction potential was not corrected. Cells were excluded if initial R_{series} was >20 M or if $V_{rest} > -60$ mV.

Histological reconstruction. In a subset of cells, biocytin (0.3%) or Alexa Fluor 594 hydrazide (50 μM) was included in the internal solution to allow morphological reconstruction. Dendritic branching was analyzed in biocytin-filled neurons. Biocytin immunohistochemistry was performed as published previously (Bender et al. 2003), and neurons were reconstructed with brightfield imaging on an Axioskop 2 plus microscope (Carl Zeiss, Thornwood, NY) and Neurolucida software (MicroBrightField, Williston, VT). Dendritic spine density was measured by manual counting in ImageJ from three-dimensional two-photon confocal stacks of Alexa Fluor-filled cells (0.2-μm *z* steps).

In vivo calcium imaging and whisker stimulation. C57BL/6J mice (age P30–P45) were anesthetized with urethane (1.2 g/kg, 10% solution in sterile saline) and chlorprothixene (0.08 mg, 4 mg/ml solution). Supplemental urethane (10% of the original dose) was given as needed. Body temperature was maintained at 37°C. In an initial surgery, a headplate was mounted that contained an aperture over S1, located 1 mm posterior and 3 mm lateral to bregma. The locations of D1, D2, and D3 cortical columns were mapped through the skull with intrinsic signal optical imaging using standard methods (Drew and Feldman 2009). A 2-mm craniotomy was made centered on the D2 column. A glass pipette (3 MΩ) loaded with OGB-1 AM (prepared as in the slice experiments above) was inserted 250 μm below the pia in the D2 column, and OGB-1 AM was bolus loaded (5 psi, 1 min). Mice were then transferred to a two-photon Moveable Objective Microscope (Sutter Instruments, Novato, CA) with a ×16, 0.8 NA objective (Nikon). Three to nine whiskers (a 3 × 1 or 3 × 3 array centered on D2) were attached to calibrated piezoelectric deflectors, which were deflected independently with custom routines in IGOR Pro (WaveMetrics). A bipolar stimulating electrode was inserted at 30° tangent to the brain surface and advanced into L4 of the imaged column, ~450–500 μm below the pia. Imaging fields with strong L4-evoked calcium responses were chosen, to ensure that imaging in L2/3 was spatially well aligned with L4 stimulation.

Imaging was performed 120–180 μm below the pia with 800-nm excitation (Chameleon, Coherent) and 525-nm emission (Chroma, HQ 525/50 filter). Detection was with a Hamamatsu photomultiplier tube (H10770PA-40). Movies of OGB-1 fluorescence (frame rate: 7.23 Hz) were collected with ScanImage (Pologruto et al. 2003) and analyzed with ImageJ (Abràmoff et al. 2004) and MATLAB. Movies were motion corrected by aligning to the mean image with the ImageJ plug-in TurboReg (Thévenaz et al. 1998), and shot noise was reduced with a 3-pixel median filter in *x*, *y*, and *t*. For each imaging field, we recorded interleaved epochs of whisker-evoked activity, L4 stimulation-evoked activity, and spontaneous activity. Whisker stimuli consisted of single whisker deflections (4° amplitude, 4-ms ramp, 100-ms hold, 4-ms return, delivered 3 mm from base) interleaved between different whiskers, with a 3- to 8-s interstimulus interval (isi). L4 stimulation consisted of single cathodal impulses, 5–80 μA, at 8-s isi.

Data were analyzed with ImageJ and MATLAB. ΔF/F traces from individual cells were calculated from ROIs manually placed over cell somata. Positive deconvolution was used to detect calcium transients in the ΔF/F signal, without thresholding. Deconvolution was calibrated by cell-attached recording in L2/3 neurons in vivo, and transients were confirmed to reflect action potentials (Clancy et al., unpublished results). Stimulus-evoked response magnitude was defined as the maximal deconvolution output in the two frames following a stimulus. Average response magnitude was computed from all presentations of the same stimulus, minus the spontaneous event magnitude measured for the same number of frames. Our goal was to test whether those neurons that were most responsive to L4 stimulation were also most responsive to principal whisker (PW) stimulation. To test this, we adjusted L4 stimulation intensity to achieve a mixture of successes and failures across trials and neurons (similar to whisker stimulation), and we only analyzed fields in which mean stimulus-evoked ΔF/F across all neurons differed less than threefold between L4 stimulation and whisker deflection.

Model. A single-compartment, parallel conductance model was used to predict the change in V_m of each cell in response to the measured excitatory and inhibitory synaptic conductances recorded in that cell. Methods were as previously described (House et al. 2011). Briefly, V_m were estimated with the difference equation (Wehr and Zador 2003):

$$V_{i+1} = -\frac{dt}{C}\left[G_e(V_i - E_e) + G_i(V_i - E_i) + G_{rest}(V_i - E_{rest})\right] + V_i$$

where capacitance C for each cell was estimated from a double exponential fit to a −5-mV step, G_e and G_i were the measured excitatory and inhibitory conductances at each time point, $E_e = 0$ mV and $E_i = -68$ mV represent the reversal potentials of G_e and G_i, $G_{rest} = 1/R_{input}$, where R_{input} was calculated with Ohm's law with a −5 mV step, and E_{rest} equaled the resting membrane potential measured immediately after breaking into the cell. The difference equation was solved in MATLAB (MathWorks) by the Runge-Kutta method with a variable time step.

Statistics. Reported values are means ± SE unless otherwise noted. All tests were performed in MATLAB. The Shapiro-Wilk test for normality was applied to all data sets. *t*-Tests and rank sum tests were used for comparisons between normal and nonnormal data, respectively. For nearest-neighbor activation threshold correlations, nonresponsive cells were assigned an activation threshold of 100%.

RESULTS

Population calcium imaging of L2/3 neuronal activity. To identify more and less responsive neurons among the L2/3 pyramidal cell population, we developed a method to image L2/3 cell spiking in response to L4 stimulation in acute S1 slices. L2/3 neurons in the center of a whisker-related cortical column were bolus loaded with the cell-permeant calcium indicator dye OGB-1 AM (Fig. 1*A*), and an extracellular stimulating electrode was placed in the L4 barrel of the same column. OGB-1 AM reliably labeled all cells in the field of view (Stosiek et al. 2003). The imaging field was located midway between the pia and the top of L4 (281 ± 8 μm from the pia for 69 slices) at a mean depth of 41 ± 1 μm in the slice.

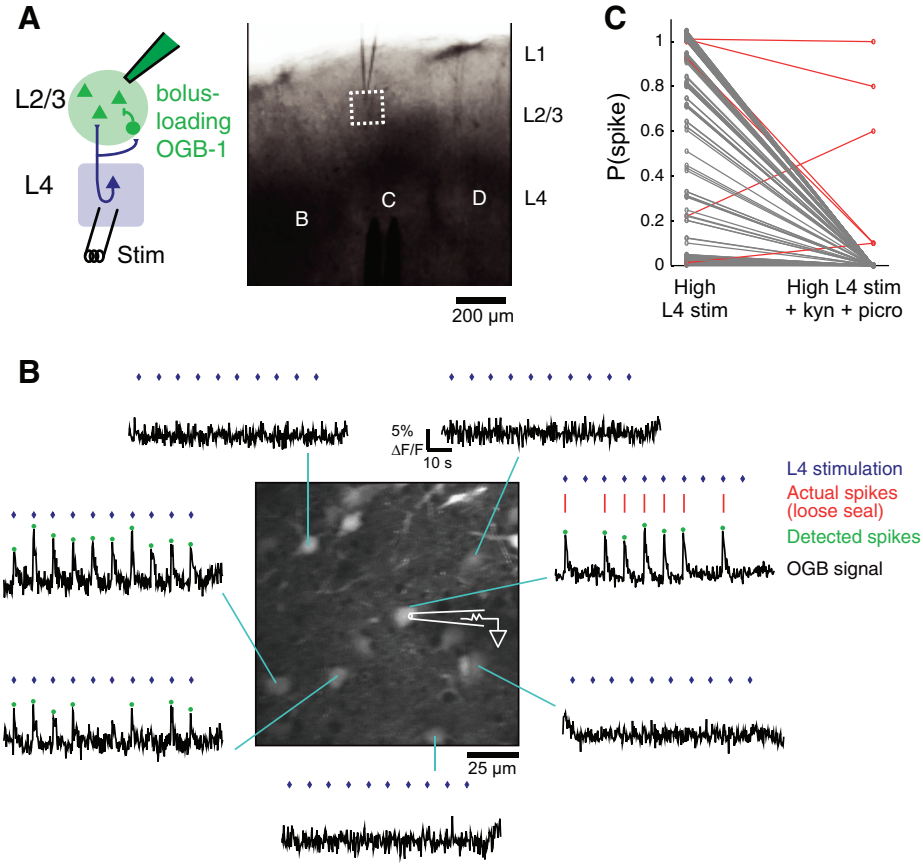

Fig. 1. L4-evoked activation of L2/3 neurons measured by population calcium imaging. *A*: the S1 slice preparation. White box shows imaging L2/3 field after Oregon Green BAPTA-1 AM (OGB-1 AM) loading. Letters indicate whisker identity of visualized barrel columns. *Inset*: schematic of the feedforward circuit. *B*: example ΔF/F traces (black) and detected spikes (green dots) from 7 neurons in a L2/3 imaging field. L4 was stimulated periodically (blue diamonds) at 17 μA intensity (corresponding to 40% of max stimulation for this column). A simultaneous loose-seal recording of spiking was made in 1 neuron (*top right*). Only a subset of cells spiked to this stimulation intensity. *C*: pharmacological test for antidromic activation of L2/3 cells. Spike probability was measured for 191 cells (14 slices), of which 148 spiked in response to strong L4 stimulation (mean 89.3 ± 0.9% normalized stimulus intensity). All but 6 cells (red) ceased spiking when kynurenic acid (kyn) and picrotoxin (picro) were added, indicating a 4% antidromic activation rate at high stimulation intensity.

This corresponds to the top of L3 (Meyer et al. 2010). Presumed glial cells were identified based on substantially brighter baseline fluorescence (Stosiek et al. 2003) and were excluded from analysis. At this depth in L2/3, neurons are 85% pyramidal cells and 15% inhibitory interneurons (Meyer et al. 2011). We used two-photon imaging to detect fluorescence transients in individual neurons in response to L4 stimulation at 0.125 Hz (Fig. 1*B*). Spike-related calcium transients were detected from the fluorescence signal by applying a nonnegative deconvolution algorithm (Vogelstein et al. 2010) to the ΔF/F trace of each cell and thresholding the resulting scores.

To calibrate our event detection method, we directly measured spikes with loose-seal recordings while monitoring OGB-1 AM fluorescence (20 pyramidal cells, 8 slices) (Fig. 1*B*). Each L4 stimulus evoked only 0 or 1 spike from each neuron. Calcium imaging detected spikes with an 82% spike detection rate and a 3% false alarm rate. This was obtained with an event detection threshold of 0.15 for deconvolution output (see MATERIALS AND METHODS), which was used for all subsequent imaging experiments. Antidromic activation of L2/3 cells was negligible, because calcium transients were abolished by the synaptic blockers kynurenic acid (2 mM) and picrotoxin (100 μM) in 96% of cells with L4-evoked spiking (142/148 cells, of 191 total cells in 14 slices) (Fig. 1*C*).

Extracellular L4 stimulation activates excitatory projections to L2/3 from L4 and L5a, with L4 being the major input to L2/3 regions over barrel column centers, which was our recording location (Shepherd et al. 2005; Shepherd and Svoboda 2005). L5b, L6, and thalamocortical axons are present but do not appreciably target L2/3 neurons at this depth (Shepherd et al. 2005; Shepherd and Svoboda 2005; Oberlaender et al. 2012). L4 stimulation will also activate feedforward disynaptic inhibition (House et al. 2011) and monosynaptic inhibitory input from L4 and L5 (Kapfer et al. 2007; Porter et al. 2001; Silberberg and Markram 2007). As L2/3 pyramidal cells begin to spike, L2/3 recurrent excitation and inhibition will also be recruited (Feldmeyer et al. 2006). Thus we interpret L4 stimulation as evoking mixed feedforward input to the L2/3 network, plus recurrent network activity as L2/3 neurons begin to spike. Computational analysis suggests that natural sensory stimulation also involves a mixture of feedforward and recurrent activation in L2/3 (Sarid et al. 2013).

A gradient of L4-evoked response probability in L2/3 neurons. We first tested whether all L2/3 neurons were recruited to spike at similar L4 stimulation intensities, or whether L4-evoked spike thresholds were broadly distributed as in hippocampus and L5 of S1 (Pouille et al. 2009). We imaged Ca signals from all neurons (mean: 14.5 cells; range: 9–21) within a 128 × 128-μm imaging field, and stimulated L4 via a stimulation electrode in the cocolumnar L4 barrel. Under our slice conditions, L4 stimulation activates feedforward excitation, feedforward inhibition, and local L2/3 recurrent circuit activation (House et al. 2011). We identified the minimal L4 stimulation intensity that evoked a small, reliable L2/3 field potential response in the center of the L2/3 imaging field (mean = 2.9 μA for 68 slices) and then stimulated at increasing intensity until L2/3 field potential amplitude saturated. To provide a consistent metric of stimulation intensity across slices, stimulation intensity was defined as the field potential amplitude (interpreted as an estimate of the average synaptic input to L2/3

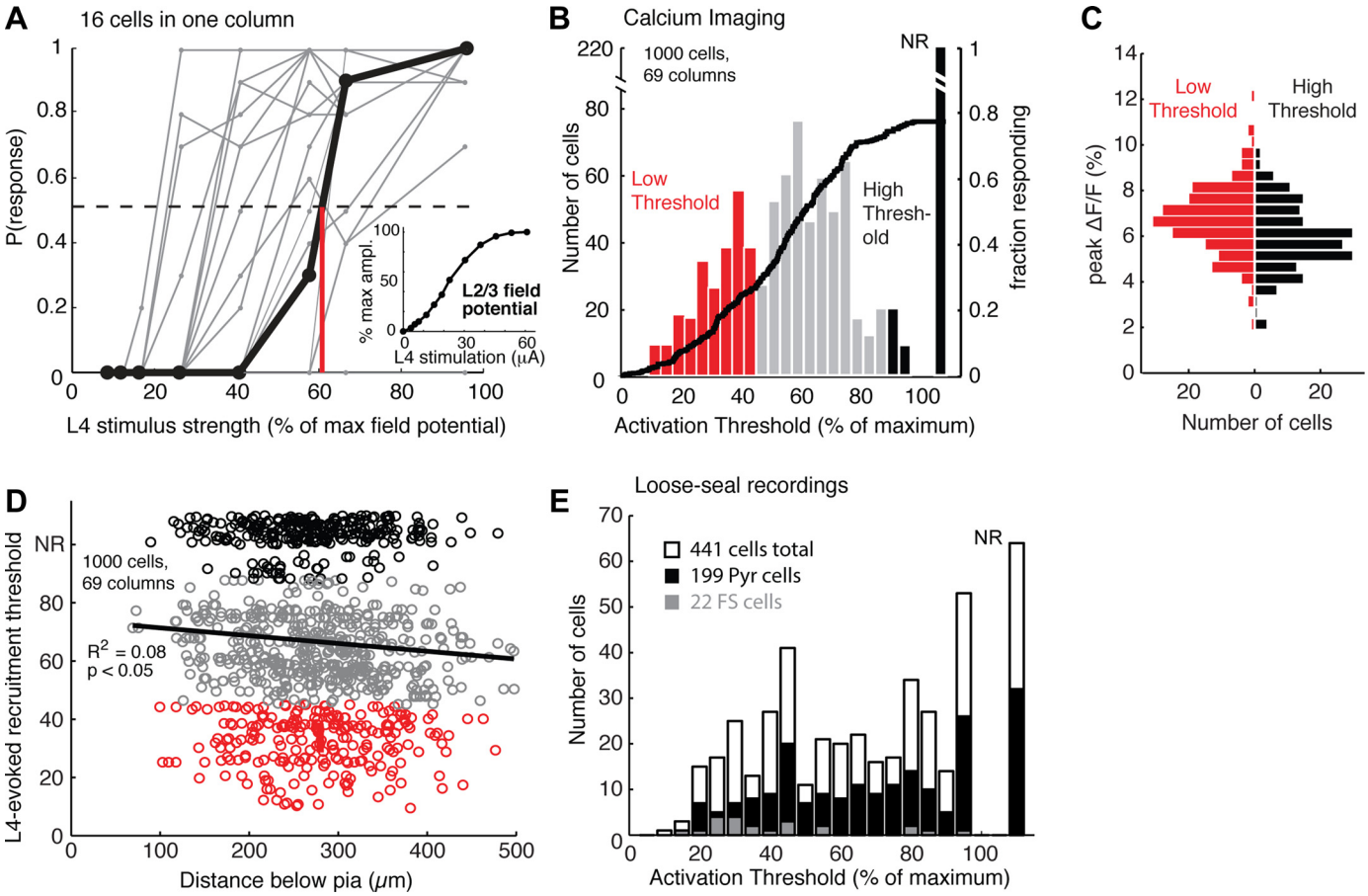

Fig. 2. Distribution of L4-evoked activation thresholds among L2/3 pyramidal cells. *A*: L4-evoked activation curves for all neurons in a single column, imaged simultaneously. Dots show L4 stimulation intensities that were tested. For the 1 neuron highlighted in black, the red line marks the activation threshold. *Inset*: method for normalizing stimulation intensity. Stimulation intensity was measured as the L2/3 field potential amplitude, normalized to the maximal (saturating) local field potential amplitude recorded in that column. *B*: distribution of activation thresholds across all cells in calcium imaging experiments. Red and black bars indicate the bottom and top quartiles of activation thresholds, which define low- and high-threshold cell populations. NR, nonresponsive. Black curve, cumulative fraction of cells responding. *C*: distribution of ΔF/F peak amplitudes for all detected calcium transients in low- and high-threshold cells. $N = 193$ low-threshold events; $N = 189$ high-threshold events; $P < 0.0001$ rank sum test; 618 cells from 69 slices. Bin size = 0.5. *D*: L4-evoked activation threshold as a function of absolute subpial depth, for all neurons. Line, linear regression. *E*: distribution of activation thresholds for all cells measured with loose-seal recordings of L4-evoked spikes. Black and gray bars, activation thresholds for physiologically and/or morphologically identified neurons (targeted as low- and high-threshold cells in the overall population). Black, confirmed pyramidal cells; gray, confirmed interneurons.

neurons) normalized to the maximal field potential amplitude for that column (Fig. 2*A*, *inset*).

Individual L2/3 neurons showed steep, saturating recruitment of L4-evoked spiking at a discrete L4 stimulus intensity (Fig. 2*A*). We defined the activation threshold of each cell as the L4 stimulation intensity that evoked 50% probability of spike-related calcium events. Activation thresholds were broadly distributed across cells, both within single columns (Fig. 2*A*) and across slices (Fig. 2*B*). This is consistent with feedforward population recruitment in CA1 hippocampus and L5 of somatosensory cortex (Pouille et al. 2009). Twenty-two percent of the cells never spiked reliably enough to define an activation threshold even at the highest stimulation intensity [i.e., *P*(spike) remained below 0.5] (Fig. 2*B*). Among responsive cells, there appeared to be a gradient of activation thresholds and no obvious clustering into discrete response classes. We therefore operationally classified cells as low threshold or high threshold using arbitrary cutoffs (activation threshold <45% or >88%, corresponding to bottom and top quartiles of activation thresholds) (Fig. 2*B*). Low- and high-threshold cells had largely overlapping peak ΔF/F amplitudes for detected events (although the means differed: 6.7% vs. 5.9%, $P < 0.0001$), confirming that these populations differed in L4-evoked spike probability, not SNR in detecting calcium events (Fig. 2*C*). The average low-threshold cell spiked when 11% of L2/3 neurons in the same field of view were firing. The average high-threshold cell never spiked, even though 78% of all neurons in the field of view were firing.

Low- and high-threshold cells (including nonresponsive cells) were spatially intermixed within the imaging field, with a cell's activation threshold showing no correlation with its nearest neighbor's activation threshold ($r = 0.03$, $P = 0.34$, 1,000 cells). Absolute subpial depth also did not differ between low-threshold cells (280 ± 5 μm, $n = 244$ cells) and high-threshold cells (270 ± 5 μm, $n = 259$ cells; $P = 0.09$). Pooled across imaging fields, there was a weak tendency for low-threshold cells to be located deeper in L2/3 (Fig. 2*D*), as expected given that L4 projects more strongly to L3 than to L2. However, this relationship explained just 8% of variance in L4-evoked activation threshold, and low- and high-threshold cells were intermixed at all depths. When subsequently

patched, nonresponsive cells exhibited healthy V_{rest}, R_{input}, and spikes evoked by somatic current injection (see below).

Calcium imaging combines pyramidal cells and interneurons, which may have lower activation thresholds (Pouille et al. 2009). To test whether a broad gradient of L4-evoked activation thresholds exists among L2/3 pyramidal cells, we performed the same experiment using loose-seal recordings to measure L4-evoked activation thresholds in many (up to 10) nearby L2/3 neurons, instead of calcium imaging. In a subset of cells, we then broke in to establish whole cell current-clamp recording with Alexa Fluor 594 (50 μM) in the internal solution and used firing patterns (Connors and Gutnick 1990) and dendritic morphology in live two-photon confocal scans to identify pyramidal cells or interneurons. Pyramidal cells were identified by characteristic dendritic morphology and dense spines; interneurons were identified by absent or low-density spines and nonpyramidal dendritic morphology (Defelipe et al. 2013). Among interneurons, we identified fast-spiking (FS) cells by multipolar primary dendrites, narrow spike widths, and sustained, nonaccommodating spiking to injected current. Both low-threshold and high-threshold neurons were overwhelmingly pyramidal cells. FS cells constituted ~10% of neurons and were biased toward low L4 activation thresholds (Fig. 2*E*).

Does the broad range of activation thresholds reflect a gradient of inherently more and less responsive L2/3 neurons, or does it reflect input specificity among an otherwise homogeneous population of neurons? Input specificity is expected because focal L4 stimulation activates only a subset of axonal inputs, which project to a subset of L2/3 neurons (Feldmeyer et al. 2002). However, there may in addition be a gradient of inherent responsiveness among L2/3 neurons, independent of the specific axonal input pathway that is activated (e.g., due to heterogeneity in intrinsic excitability, recurrent connectivity, or feedforward synaptic properties) (Benedetti et al. 2013; Yassin et al. 2010). To test whether some component of the response gradient was stimulus pathway independent, we performed a two-pathway experiment in which we stimulated in both the cocolumnar L4 barrel (*pathway 1*) and an adjacent L4 barrel (*pathway 2*) (Fig. 3*A*). Because L4 cells extend very few dendrites or axons into neighboring barrels (Petersen and Sakmann 2000), these two stimulation sites activate distinct L4 inputs to the L2/3 imaging field, with the cocolumnar input providing substantially stronger input than adjacent column input (Feldmeyer et al. 2013). We measured L4-evoked spiking of L2/3 neurons on both pathways and then rank-ordered cells according to their activation thresholds on each pathway (Fig. 3*B*). If activation thresholds depended only the on the specific presynaptic axons that are stimulated, there should be no correlation in responsiveness between home-barrel and adjacent-barrel stimulation. Cells showed greater responsiveness to home-barrel than adjacent-barrel stimulation, consistent with the largely columnar architecture of the L4-L2/3 projection (Bender et al. 2003; Bureau et al. 2004) (Fig. 3*B*). However, a significant correlation existed between activation threshold rankings on the two pathways (4 slices, $P < 0.0001$, $R^2 = 0.30$; Fig. 3*C*), with the same subset of neurons tending to be recruited at lower activation thresholds on both pathways. This indicates that, in addition to input specificity, inherent differ-

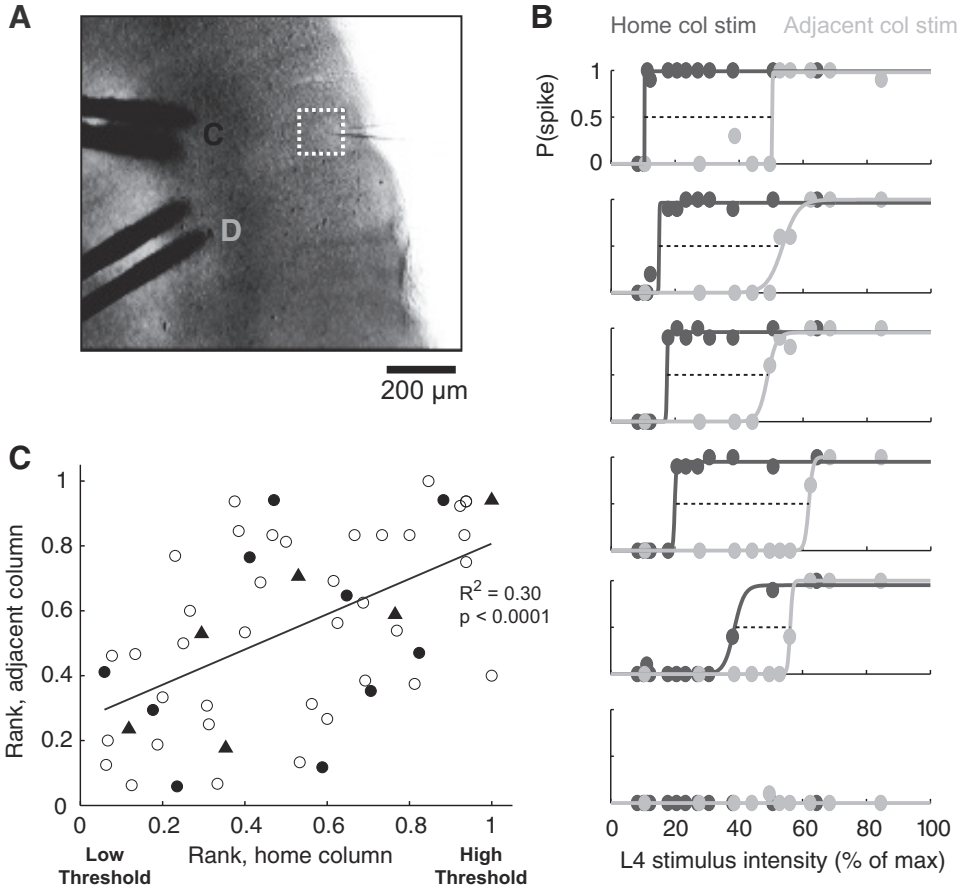

Fig. 3. Comparison of activation thresholds on 2 stimulation pathways. *A*: stimulation electrodes and imaging field for a 2-pathway experiment. The field potential recording electrode (for stimulus normalization) is shown in the center of the imaging field. *B*: L4-evoked spiking recruitment for 6 cells, all imaged simultaneously in the same field. Dark gray, spike probability in response to home-column stimulation; light gray, adjacent-column stimulation. Dashed lines connect activation thresholds on both pathways. Cells are ordered by home-column activation threshold. *C*: correlation between activation thresholds (ranked within each imaging field) for home- and neighboring-barrel stimulation (54 cells, 4 slices). Filled symbols show all cells in 1 example experiment (triangles are the 6 cells in *B*).

ences in L4-evoked responsiveness exist between L2/3 neurons that contribute to the gradient of L4-evoked spike thresholds.

Intrinsic excitability is inversely related to L4-evoked spike probability. To identify the cellular mechanisms underlying the gradient of activation thresholds, we first tested for differences in intrinsic excitability among L2/3 pyramidal cells. We measured L4-evoked activation threshold using loose-seal recordings of L4-evoked spikes and classified low-threshold and high-threshold cells using the stimulus intensity criteria in Fig. 2*B*. We then broke in to establish whole cell recording mode, identified pyramidal cells by regular spiking responses to current injection (Connors and Gutnick 1990) and morphology, and characterized intrinsic membrane properties. Only pyramidal cells were included in this and all subsequent in vitro experiments.

Surprisingly, low-threshold pyramidal cells were overall less intrinsically excitable than high-threshold pyramidal cells (Figs. 4 and 5 and Table 1). Low-threshold cells had more depolarized spike thresholds than high-threshold cells (-35.5 ± 0.5 vs. -37.1 ± 0.4 mV, $P < 0.01$) and showed a trend for more hyperpolarized V_{rest} (-74.6 ± 0.5 vs. -73.3 ± 0.6 mV, $P = 0.059$) (Fig. 4, *A* and *B*). As a result, the depolarization required to reach spike threshold from V_{rest} was greater in low-threshold cells than in high-threshold cells (39.1 ± 0.7 vs. 36.2 ± 0.6 mV, $P < 0.01$). The small difference in V_{rest} was not due to differences in I_h, which is minimal in L2/3 neurons (Fig. 4*C*). Low- and high-threshold cells showed no difference in R_{input} or C_m (Fig. 4*D* and Table 1). Subpial depth was identical for low-threshold and high-threshold cells in these experiments (Table 1).

We next examined the *F-I* relationship in response to 500-ms current injection (Fig. 5*A*). There was no difference in rheobase between low- and high-threshold cells [254 ± 11 pA vs. 273 ± 14 pA, not significant (n.s.)] (Fig. 5*B*). High-threshold cells spiked slightly, but significantly, more as a function of injected current above rheobase compared with low-threshold cells (e.g., 9.9 ± 0.6 spikes at rheobase + 240 pA for high-threshold cells vs. 9.6 ± 0.3 spikes for low-threshold cells, $P < 0.0001$, 2-way ANOVA). While all pyramidal cells exhibit an adapting spike pattern in response to current injection, some pyramidal cells tend to produce an initial high-frequency spike doublet at spike train onset. We found that this doublet spiking behavior varied between low- and high-threshold cells, with high-threshold cells exhibiting

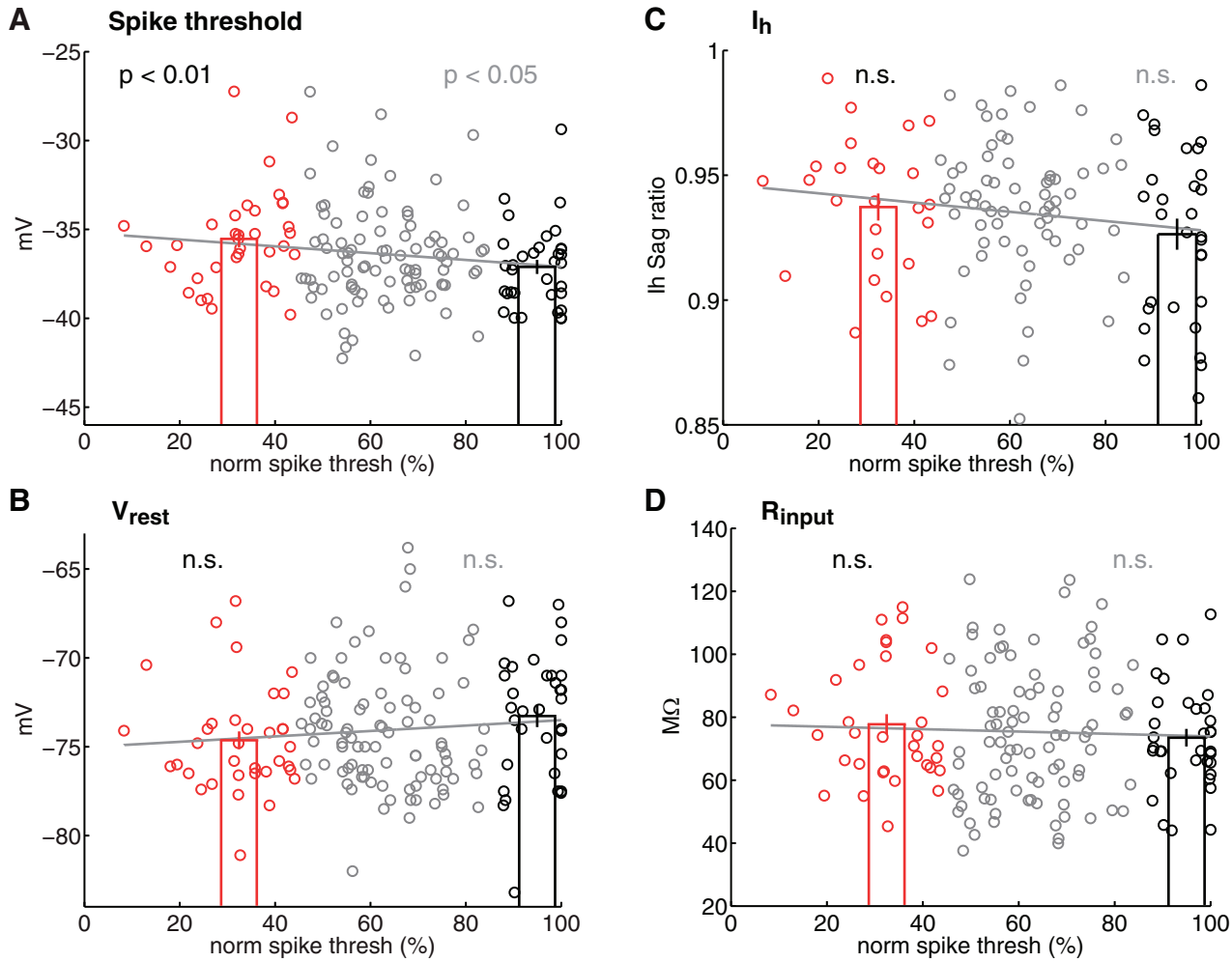

Fig. 4. Intrinsic excitability varies with L4 activation threshold. *A* and *B*: spike threshold and resting potential (V_{rest}) for all neurons ($n = 160$ cells). n.s., Not significant. *C*: I_h measured as membrane potential (V_m) sag ratio in response to a 500-ms, −200-pA current step from V_{rest}. $n = 124$ cells. *D*: input resistance (R_{input}) for all cells ($n = 158$ cells). For all panels, red symbols are low-threshold cells and black symbols are high-threshold cells. Black *P* values show 2-group comparison between low- and high-threshold cells. Gray *P* values are for linear regressions for all cells, including cells with intermediate activation thresholds (gray lines). Bars show means ± SE.

Table 1. *Physiology of low- and high-threshold pyramidal cells*

Properties	Low Threshold (35 cells)	High Threshold (34 cells)	*P* Value
Burst step, pA above rheobase	274 ± 13	173 ± 16	<0.0001
Burst step, absolute pA	528 ± 13.7	436 ± 21	<0.001
Spike threshold, mV	−35.5 ± 0.5	−37.1 ± 0.4	<0.01
Spike threshold − V_{rest}, mV	39.1 ± 0.7	36.2 ± 0.6	<0.01
V_{rest}, mV	−74.6 ± 0.5	−73.3 ± 0.6	0.059
Rheobase, pA	254 ± 11	273 ± 14	n.s.
Sag ratio (I_h) (26 and 30 cells), mV	1.0 ± 0.1	1.3 ± 0.1	n.s.
C_m, pF	279 ± 16.8	288 ± 27.7	n.s.
mAHP magnitude, mV	−5.4 ± 0.3	−5.8 ± 0.3	n.s.
R_{input}, MΩ	77.8 ± 3.2	73.5 ± 2.8	n.s.
Age, days	19 ± 0.3	20 ± 0.2	n.s.
Recording depth, μm	68.1 ± 2.1	71.6 ± 2.6	n.s.
Distance below pia, μm	320.9 ± 11.6 (34 cells)	315.2 ± 13.2 (29 cells)	n.s.

Values are means ± SE. Burst step, current injection required to evoke an initial spike doublet with <10-ms interspike interval; V_{rest}, resting potential; C_m, membrane capacitance; R_{input}, input resistance; n.s., not significant.

spike doublets at lower current injections (Fig. 5, *A* and *C*). This difference was observed both as an increase in firing rate of the first two spikes at 240-pA current injection (Fig. 5*D*) and a decrease in the current amplitude required to elicit an initial doublet with <10-ms ISI (Fig. 5*E*). Thus L2/3 pyramidal cells that are less effectively driven by feedforward synaptic input exhibit lower spike threshold and a greater tendency for an initial doublet burst.

To test whether these differences in intrinsic excitability reflect distinct subpopulations of more and less responsive cells, or a smooth gradient across pyramidal cells, we also measured intrinsic properties for neurons with intermediate L4 activation thresholds. All intrinsic properties that were different between low- and high-threshold populations showed a smooth gradient as a function of L4-evoked activation threshold (Figs. 4 and 5). This contrasts with CA1 and L5 of rodent S1, which contain discrete pyramidal cell subtypes with well-separated physiological properties including initial firing frequency (Graves et al. 2012; Hattox and Nelson 2007).

Low- and high-threshold cells differ in L4-evoked excitation but receive similar inhibition. Spike probability to sensory stimulation is also determined by the balance between excitatory and inhibitory synaptic inputs (Crochet et al. 2011; Moore and Nelson 1998). Thus more responsive L2/3 pyramidal cells may have larger L4-evoked excitatory synaptic conductance (G_e), as observed in CA1 and L5 of S1 (Pouille et al. 2009), or larger G_e coupled with smaller L4-evoked inhibitory synaptic conductance (G_i), as observed for fosGFP+ L2/3 pyramidal cells in the fosGFP mouse (Benedetti et al. 2013). To directly measure G_e and G_i in low- and high-threshold cells, we first identified low- or high-threshold L2/3 cells with OGB imaging and then performed whole cell voltage-clamp recordings. Only pyramidal cells were studied, as determined by live two-photon imaging of dendritic morphology (Fig. 6*A*, *top*). We stimulated in L4 at an intermediate stimulus intensity (normalized stimulation intensity for 17 slices: 46.9 ± 3.7%), so that only a minority of cells were responsive in the field. We recorded L4-evoked synaptic currents at this stimulation intensity, using a range of V_{hold} to allow estimation of L4-evoked G_e and G_i (Fig. 6*A*, *bottom*; see MATERIALS AND METHODS).

Low-threshold cells ($n = 22$) had significantly larger peak G_e than high-threshold cells ($n = 14$) (29.2 ± 3.0 vs. 17.7 ± 1.3 nS, $P < 0.001$; Fig. 6*B*). G_i was larger than G_e for all cells, as expected given the existence of prominent L4-L2/3 feedforward inhibition, recurrent local L2/3 inhibition, and monosynaptic L4-L2/3 and L5-L2/3 inhibition in this circuit (House et al. 2011; Kapfer et al. 2007; Porter et al. 2001; Shao et al. 2013; Silberberg and Markram 2007). Peak G_i was not significantly different between low- and high-threshold cells (116.6 ± 14.4 vs. 107.7 ± 16.1 nS, n.s.). Identical results were found for integrated conductance (data not shown). Low-threshold cells had faster G_e onset latency (2.8 ± 0.1 vs. 3.2 ± 0.1 ms, $P < 0.05$) and a trend for faster G_i onset latency (3.0 ± 0.1 vs. 3.4 ± 0.2 ms, $P = 0.08$). To understand how these differences in synaptic conductance would affect overall postsynaptic potentials (PSPs), we predicted the PSP that would result from the measured G_e and G_i waveforms for each cell, modeled as inputs into a single-compartment model (Fig. 6*C*; see MATERIALS AND METHODS). The predicted peak PSP was significantly larger in low-threshold cells relative to high-threshold cells (peak V_m: −55.6 ± 0.8 vs. −59.5 ± 1.3 mV, $P < 0.05$; Fig. 6*C*, *right*). This larger G_e is consistent with higher L4-evoked spike probability in low-threshold cells.

Low- and high-threshold cells have similar dendritic morphology and spine density. In L5 of S1 and CA1 hippocampus, physiologically distinct pyramidal cell classes are also characterized by differences in apical and basal dendritic morphology (Graves et al. 2012; Hattox and Nelson 2007). In L2/3 of rodents, L2 and L3 pyramidal cells differ in apical dendritic morphology and are intermixed at the L2-L3 border (Oberlaender et al. 2012), but physiological specialization between these classes is not known. We tested whether low- and high-threshold pyramidal cells differed in dendritic morphology by filling neurons with biocytin and analyzing neurons with complete dendritic reconstructions ($n = 12$ and 12 cells) (Fig. 7*A*). Low- and high-threshold cells did not differ in soma area, total basal dendritic length, total apical dendritic length, or apical dendritic trunk diameter (Table 2). The groups did not differ significantly in subpial depth (Table 2). Sholl analysis of basal dendrites revealed no difference in dendritic length as a function of distance from the soma (Fig. 7*B*, *left*). Sholl analysis of apical dendrites showed a modest difference in apical dendrite distribution, with a greater proportion of dendritic length contained in the distal tuft for high-threshold cells (2-sided Kolmogorov-Smirnov test, $P < 0.01$; Fig. 7*B*, *right*).

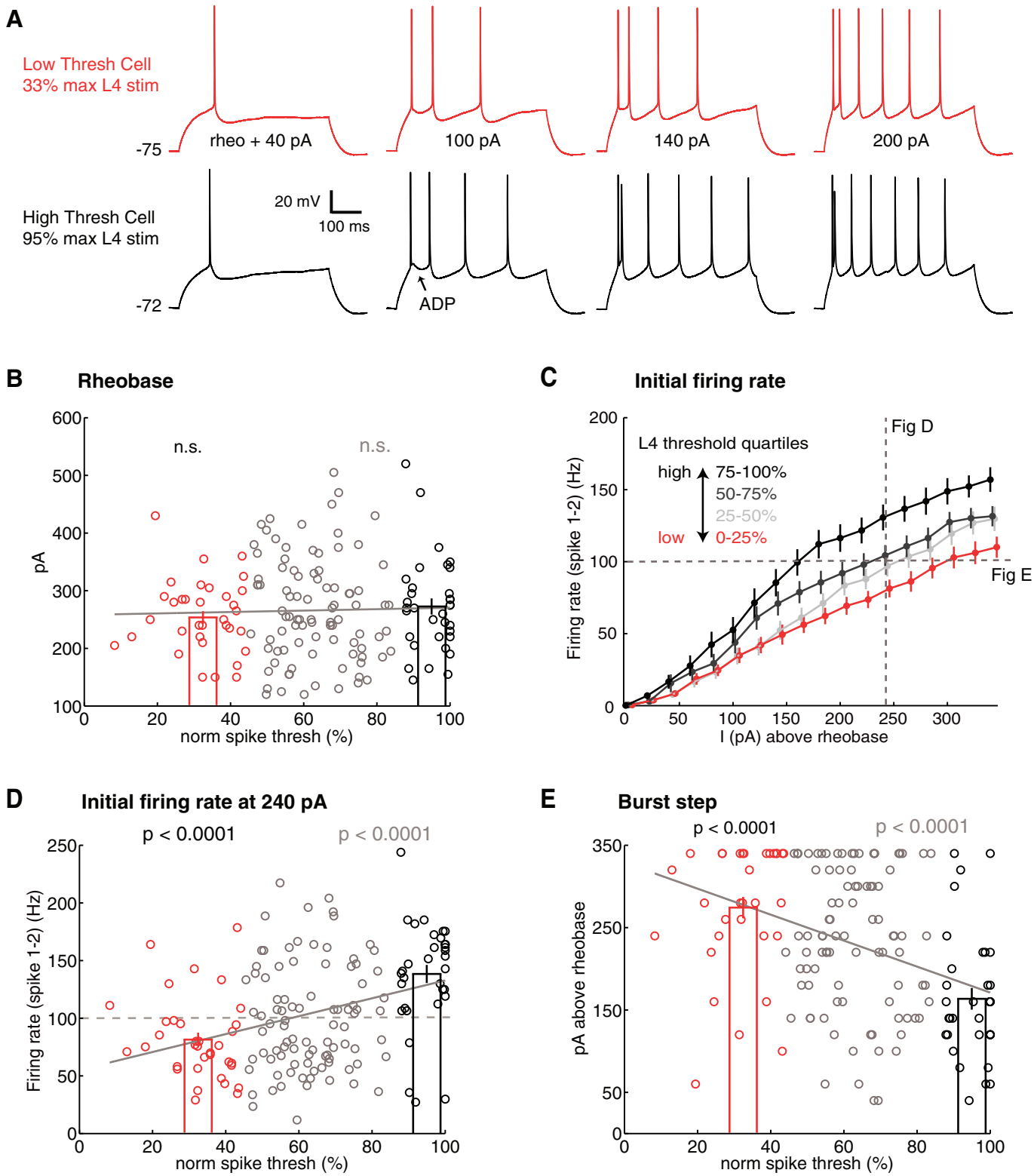

Fig. 5. Initial doublet spiking is inversely related to L4-evoked responsiveness. *A*: example firing patterns in response to 500-ms current injection from V_{rest}. The high-threshold cell generates a higher-frequency initial doublet at 140–200 pA. ADP, afterdepolarization. *B*: rheobase for all cells (n = 160). *C*: firing rate of first 2 spikes [inverse of first interspike interval (ISI)] as a function of current injection amplitude, for all cells (n = 160). Cells are divided into quartiles of L4-evoked activation threshold (n = 34–50 cells/group). Dashed lines show comparisons plotted in *D* and *E*. *D*: firing rate for first 2 spikes for current injection of 240 pA above rheobase, for all cells (n = 160). *E*: current injection (above rheobase) required to elicit a first ISI of ≤10 ms, termed the "burst step," for all cells (n = 160). Conventions for colors and *P* values are as in Fig. 4. Bars indicate means ± SE.

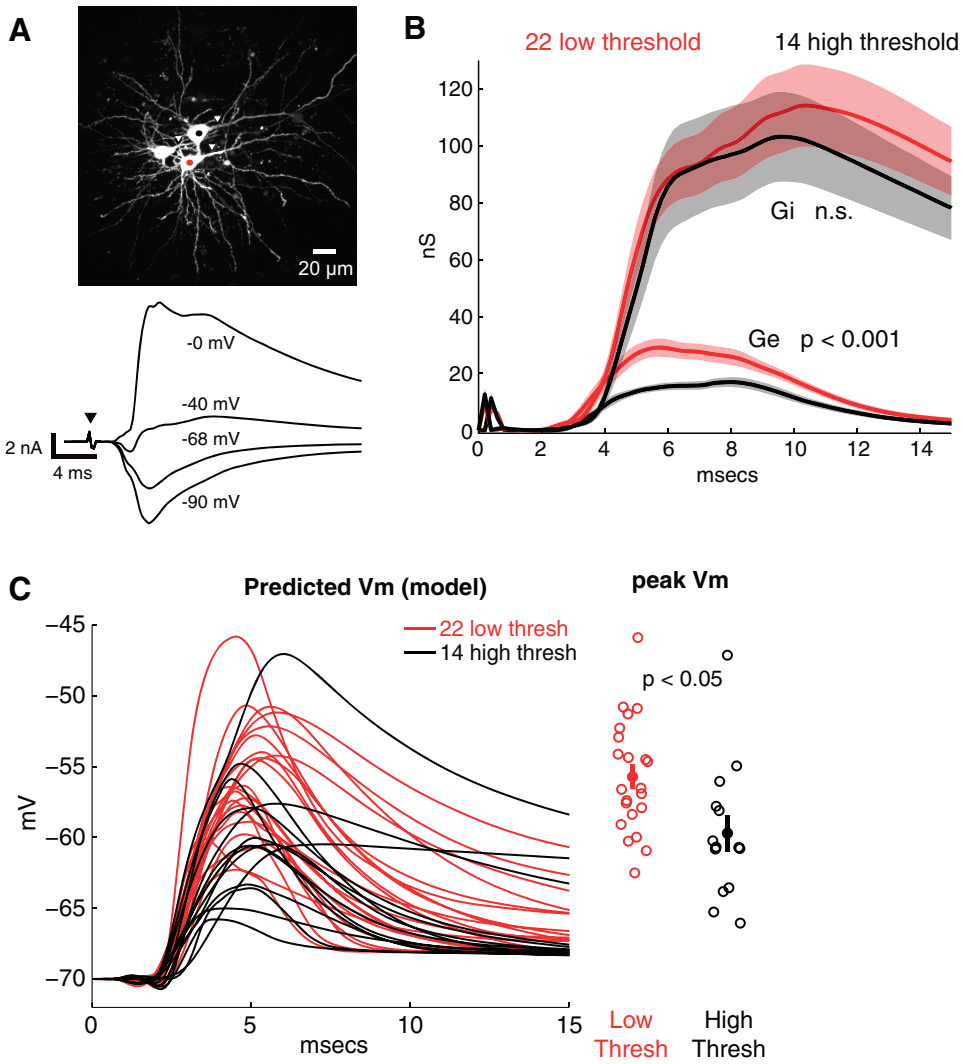

Fig. 6. Excitatory (G_e) and inhibitory (G_i) synaptic conductances in low- and high-threshold pyramidal cells. *A*, *top*: 3 cocolumnar pyramidal cells filled with Alexa Fluor 594. Red and black dots indicate low- and high-threshold cells. Arrowheads show apical dendritic trunks. *Bottom*: example currents from a synaptic conductance recording of a low-threshold cell, averaged across 5 sweeps. Cell was stimulated at its activation threshold of 37.6% maximum L4 stimulation. Arrowhead indicates L4 stimulation. *B*: average G_e and G_i waveforms measured in low-threshold (red) and high-threshold (black) cells. Shading indicates SE. L4 was stimulated at 0 ms. *C*, *left*: postsynaptic potential (PSP) predicted for each cell with a single-compartment model, based on the actual G_e and G_i waveforms measured in each cell. *Right*: predicted PSP peak for each low-and high-threshold cell (open symbols). Filled symbols are means ± SE.

These trends were also true for basal and apical dendritic branch points (data not shown). Whether this modest difference in apical dendrite morphology is functionally relevant is unknown.

We also examined dendritic spine density. We identified low- and high-threshold cells using either OGB imaging or loose-seal recordings and then patched neurons with internal solution containing Alexa Fluor 594. After allowing 10 min to achieve bright dendritic labeling, we made two-photon confocal scans of basal dendrites and quantified linear spine density on multiple second- and third-order basal branches for each cell. These branches receive the majority of L4 excitatory input (Lübke et al. 2003). We plotted spine density for each branch vs. the cell's L4 activation threshold (Fig. 7*D*). Individual branches within a single cell varied in spine density (vertical spread at a given L4 threshold in Fig. 7*D*). Despite a modest, nonsignificant trend for lower spine density with increasing L4 activation threshold (Fig. 7*D*; $P = 0.07$, regression line), there was no significant difference in spine density between the two populations of low- vs. high-threshold cells (Table 2). Thus these analysis revealed no substantial differences in dendritic morphology, soma size, or spine density between low- and high-threshold cells.

Does L4-evoked activation threshold correlate with sensory responsiveness in vivo? In vivo, L2/3 neurons exhibit a range of responsiveness to whisker stimulation (Crochet et al. 2011; de Kock et al. 2007; Kerr et al. 2007; O'Connor et al. 2010a; Sato et al. 2007). To test whether cells identified by low-threshold L4 activation represent the more whisker-responsive cells in vivo, we performed two-photon calcium imaging experiments in L2 of anesthetized mice in vivo (Fig. 8, *A* and *B*). Mice were chosen because of technical considerations including less brain pulsation, which allows for more stable in vivo imaging. We focused on L2, rather than upper L3 as in the slice experiments, because L2 provides superior signal detection for imaging. OGB-1 AM was bulk loaded into L2/3 in vivo. Fluorescence imaging (7.23-Hz frame rate) was performed in a 110- to 160-μm square imaging field, located in L2/3 130–180 μm (average 145 μm) below the pia, and $\Delta F/F$ traces were calculated from ROIs drawn over individual neuronal somata. Whisker-evoked calcium transients (Fig. 8*C*) were measured in response to single-whisker deflections (4° amplitude), applied separately to three to nine neighboring whiskers (30–100 repetitions per whisker, interleaved, at 3- to 8-s isi). Spike-related calcium transients were detected by positive deconvolution of the $\Delta F/F$ traces. For each neuron, we

calculated the average response magnitude to deflection of the PW (defined as the whisker that evoked the greatest response)

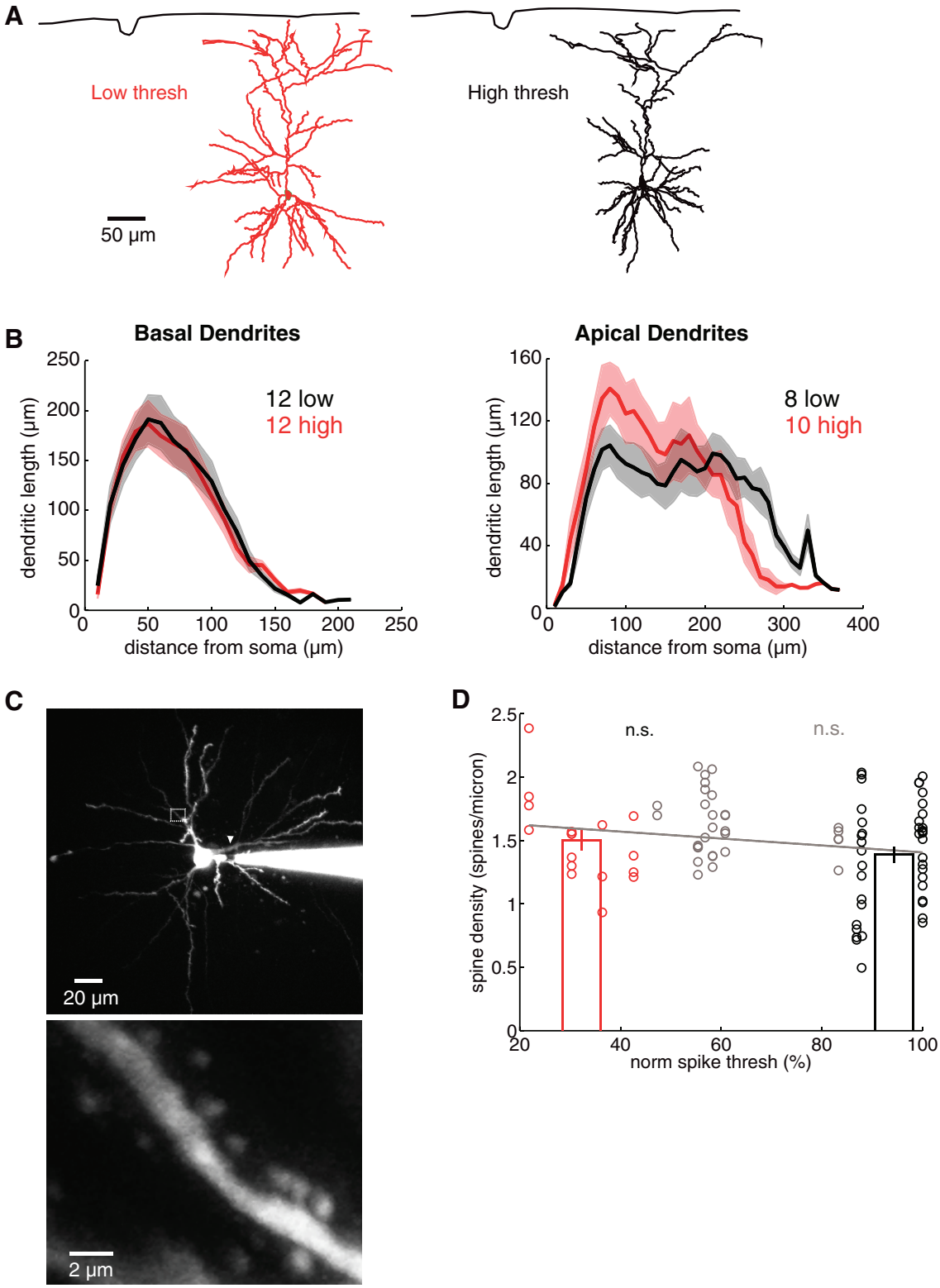

Fig. 7. Dendritic morphology and spine density in low- and high-threshold cells. *A*: Neurolucida reconstructions of a low (red)- and a high (black)-threshold cell from the same slice. *B*: Sholl analysis showing mean dendritic length in radial 10-μm bins around the soma. Cell numbers are indicated. Shading indicates mean ± SE across neurons. *C*: example of Alexa Fluor 594-filled high-threshold pyramidal cell. Arrowhead indicates apical trunk. A tertiary basal dendrite is boxed and enlarged at *bottom* to show spines. *D*: spine density for each analyzed basal branch, plotted vs. the activation threshold for each cell (89 branches from 20 cells). Red and black points are branches on low- and high-threshold cells. Bars indicate means ± SE.

Table 2. *Morphology of low- and high-threshold pyramidal cells*

Properties	Low Threshold (12 cells)	High Threshold (11 cells)	*P* Value
Soma area, μm^2	166 ± 9	145 ± 14	n.s.
Soma distance from pia, μm	285 ± 22	256 ± 16	n.s.
Distance, soma to first apical branch point, μm	22.0 ± 3.0	28.2 ± 3.3 (10 cells)	n.s.
Apical trunk thickness, μm	2.5 ± 0.2	2.4 ± 0.2 (10 cells)	n.s.
Total basal dendritic length, μm	1,691 ± 188	1,741 ± 254	n.s.
Total apical dendritic length, μm	1,909 ± 217	2,071 ± 173	n.s.
Ratio of apical to basal total length	1.20 ± 0.14	1.59 ± 0.36	n.s.
Basal spine density, spines/μm	1.45 ± 0.13 (4 cells)	1.38 ± 0.11 (9 cells)	n.s.

Values are means ± SE. Apical trunk thickness, diameter measured 15 μm from soma center.

and to L4 stimulation, delivered via an electrode in L4 of the imaged column. Spontaneous event magnitude was subtracted. L4 stimulation intensity was adjusted so that most neurons exhibited a mixture of responses and failures across trials. L4 stimulation is likely to activate L2 neurons via a mixture of feedforward pathways, including the paralemniscal L5a → L2 pathway that is prominent in mice (Bureau et al. 2006).

Different neurons exhibited a range of average response magnitudes to PW deflection and L4 stimulation. We compared the response magnitude for each neuron in the imaging field to PW deflection vs. L4 stimulation (132 cells, 6 imaging fields, 4 mice). To compare responses across stimuli and between neurons, we normalized all response magnitude values to the PW-evoked response magnitude of the most responsive neuron in each imaging field. Thus 0 indicates a nonresponsive neuron, and 1 indicates the strongest whisker-evoked response magnitude for any cell in the field. While L4 stimulation evoked higher response probability, on average, than PW deflection, we observed a significant correlation between L4-evoked response strength and PW-evoked response strength across neurons ($R^2 = 0.44$, $P < 1 \times 10^{-5}$). That is, the same subset of cells tended to respond most strongly to both whisker and L4 stimulation (Fig. 8*D*). Thus L4-evoked responsiveness predicts sensory responsiveness, and therefore the cellular properties that determine the gradient of feedforward responsiveness are likely to contribute to the gradient of whisker responsiveness in L2/3 in vivo.

DISCUSSION

In S1 in vivo, a small subpopulation of L2/3 pyramidal neurons are more active and provide most whisker-evoked spikes (Crochet et al. 2011; de Kock et al. 2007; de Kock and Sakmann 2009; Kerr et al. 2007; Margolis et al. 2012; O'Connor et al. 2010a; Sato et al. 2007). What cellular and circuit factors underlie this sparse, nonuniform sensory code is actively debated (Barth and Poulet 2012). In addition to cell-specific sensory tuning (Andermann and Moore 2006; Este-

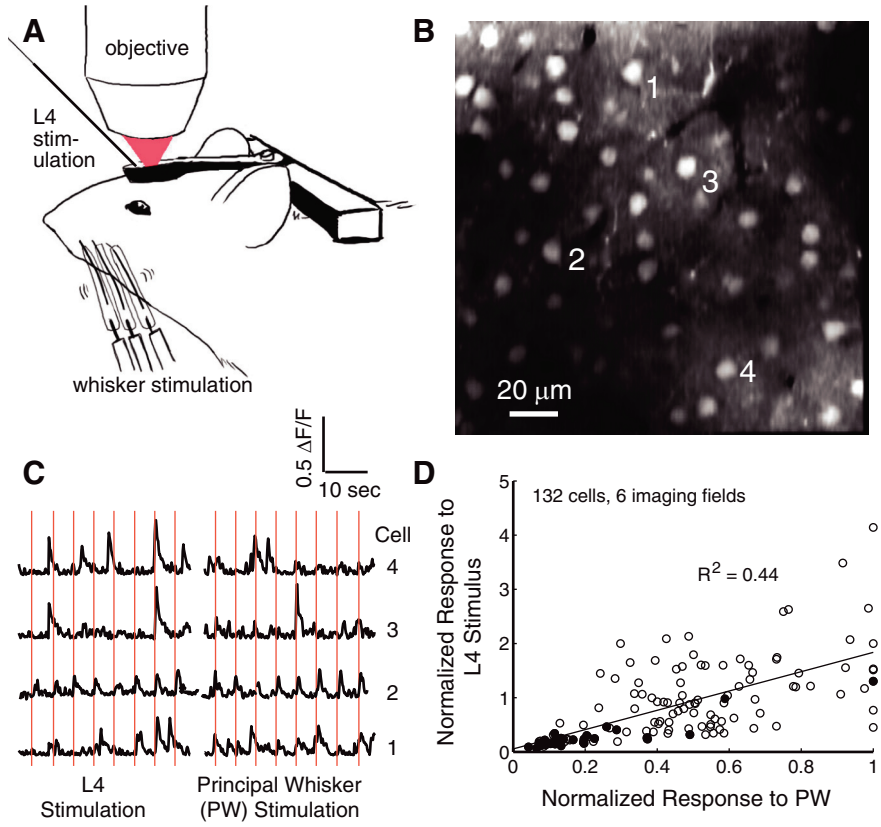

Fig. 8. Correlation between L4-evoked and whisker-evoked responsiveness in vivo. *A*: experimental setup for 2-photon calcium imaging of L2/3 pyramidal cells in the anesthetized mouse. Calcium transients were measured in response to both whisker stimulation and direct electrical stimulation of L4. *B*: example field of view after bolus loading with OGB-1 AM in a P36 mouse. *C*: ΔF/F traces from 4 cells (labeled *1–4* in *B*) during repeated L4 stimulation (*left*) and deflection of the principal whisker (PW; *right*). Vertical red lines indicate stimulation times. *D*: comparison of responses to electrical and whisker stimulation for each neuron ($n = 132$ cells, $n = 6$ fields, 4 animals). Filled points indicate cells from a single case.

banez et al. 2012) and variation in excitation-inhibition (E-I) ratio (Crochet et al. 2011), specialized subsets of pyramidal neurons may exist that have inherently lower vs. higher responsiveness, independent of sensory tuning (Barth and Poulet 2012). This model is strongly supported by the existence of a highly spontaneously active subset of pyramidal cells that preferentially synapse in a mutually interconnected network (Benedetti et al. 2013; Yassin et al. 2010), and by the finding that sensory responsiveness varies between L2/3 neurons with different long-distance projection targets (Sato and Svoboda 2010). However, whether more and less active pyramidal neurons represent distinct cell classes or the extremes of a response gradient, and what cellular and local circuit factors differentiate these neurons, was unclear.

Response heterogeneity assayed by feedforward synaptic activation. Prior studies of L2/3 response heterogeneity focused on mice that express the activity-dependent fosGFP transgene, which marks strongly active neurons in vivo (Barth et al. 2004; Benedetti et al. 2013; Yassin et al. 2010). fosGFP+ and fosGFP− neurons differ in local connectivity, intrinsic excitability, and synaptic input, including L4-evoked feedforward excitation (Benedetti et al. 2013; Yassin et al. 2010). Whether fosGFP+ and fosGFP− neurons represent two distinct cell classes, or the tails of a broad response gradient among L2/3 pyramidal cells, was unclear.

We took an unbiased functional approach, rather than a genetically targeted approach, to determine the distribution of responsiveness among all L2/3 pyramidal cells in a local region. We measured spiking recruitment of L2/3 pyramidal cells in response to L4 stimulation, which reflects a combination of feedforward synaptic activation by L4 → L2/3 and L5a → L2/3 pathways as well as L2/3 recurrent circuits activated as L2/3 neurons begin to spike. Thus spiking responsiveness of individual L2/3 neurons reflects the strength and dynamics of feedforward and local recurrent circuits, as well as intrinsic excitability. L4-evoked activation thresholds were distributed broadly across nearly the entire dynamic range of input strength, as determined by the magnitude of L4-evoked field potential in L2/3 (Fig. 2). This gradient of spiking recruitment was correlated with gradients of synaptic and biophysical properties (Figs. 4–6) and was statistically correlated across distinct L4 stimulation sites with an R^2 value of 0.3 (Fig. 3). This indicates that a gradient of responsiveness exists across L2/3 pyramidal cells during network recruitment, which is partially independent of tuning for specific feedforward inputs. We did not observe discrete more and less responsive cell populations, although these may have been obscured by variation in circuit integrity following slice preparation or other experimental variables.

In separate experiments in mice in vivo, responsiveness of L2 pyramidal cells to L4 stimulation correlated with responsiveness of the same cells to PW stimulation (Fig. 8). This suggests that the gradient of feedforward responsiveness among L2/3 neurons contributes to the heterogeneity of whisker-evoked response magnitude in vivo. Together, these parallel findings in rat brain slices and in mice in vivo support the idea that a gradient of responsiveness exists across L2/3 neurons independent of specific stimulation pathway.

Cellular correlates of responsiveness among L2/3 pyramidal cells. The recruitment gradient among L2/3 pyramidal cells is likely to reflect both circuit and cellular factors. Circuit factors may include dominance of different types of input in different neurons (e.g., low-threshold and high-threshold cells may receive differential input from specific feedforward, recurrent, or top-down feedback pathways). Cellular factors may include variation in total excitatory input strength from all sources or in intrinsic excitability. Here we focused on cellular correlates of spiking responsiveness.

Activation thresholds among L2/3 pyramidal cells were not explained by passive electrophysiological properties (R_{input}, C_m, V_{rest}) but correlated with several synaptic and biophysical features. Low-threshold (more responsive) neurons received stronger L4-evoked excitation than high-threshold neurons but the same amount of L4-evoked inhibition (Fig. 6). Such cell-specific excitation and homogeneous inhibition is found in feedforward projections to L5 and CA1 (Pouille et al. 2009). This suggests that cell-specific reversal potentials observed for whisker-evoked synaptic responses in L2/3 neurons in vivo are likely to reflect variation in whisker-evoked excitation, rather than inhibition, across L2/3 neurons (Crochet et al. 2011). In contrast, fosGFP+ (low threshold) neurons in young mice (P12–P14) receive both more feedforward excitation and less feedforward inhibition than fosGFP− cells (Benedetti et al. 2013). This difference in inhibitory input may be a transient feature of the developing L4-L2/3 projection.

Most strikingly, pyramidal cells with low L4-evoked activation thresholds (more responsive cells) had higher (more depolarized) spike threshold, required greater depolarization (spike threshold − V_{rest}) to reach spike threshold, and were less likely to generate an initial doublet spike burst in response to somatic current injection (Fig. 5). Thus more responsive cells were less intrinsically excitable, confirming findings from fosGFP+ and fosGFP− cells (Yassin et al. 2010). The significant inverse correlation between L4 responsiveness and intrinsic excitability demonstrates that the gradient of L4-evoked activation thresholds was not an artifact of the acute slicing procedure, or of placement of the L4 stimulating electrode. In these cases, there would be no systematic relationship between L4 responsiveness and intrinsic excitability. One possibility is that homeostatic plasticity adjusted intrinsic excitability for each cell in vivo to compensate for variations in mean spiking activity (Desai et al. 1999; Lambo and Turrigiano 2013; Yassin et al. 2010), as suggested previously (Yassin et al. 2010).

The biophysical basis for these differences in intrinsic excitability is not known. Doublet spiking in L2/3 neurons is caused when a backpropagating somatic spike interacts with dendritic depolarization to elicit a brief dendritic calcium spike (Larkum et al. 2007). More doublet spiking in high-threshold cells could therefore reflect higher density of dendritic Ca^{2+} or Na^+ channels, less dendritic K^+ conductance, or tighter dendrite-soma electrical coupling. Alternatively, these cells could receive a larger fraction of synaptic excitation in the distal dendrite, which would promote dendritic spiking. Differences in low-voltage-activated conductances are also suggested by the finding that low- and high-threshold cells differed in the depolarization necessary to reach spike threshold from V_{rest} but had identical R_{input} and rheobase. This suggests that these cells may differ in low-voltage-activated conductances that do not contribute to R_{input} near V_{rest} but influence V_m closer to spike threshold.

L2/3 pyramidal cells exhibit a range of dendritic morphology, and distinct L2 vs. L3 morphological classes have

been reported in rat S1 that are intermixed at mid-L2/3 depths (Oberlaender et al. 2012). Whether these morphological classes are also physiologically distinct, as in primate L2/3 (Zaitsev et al. 2012), is unclear. We found no major morphological distinctions in dendrites or somata between low- and high-threshold L2/3 pyramidal cells (Fig. 7). This included soma size, basal dendrite and distribution, apical dendrite length and trunk diameter, apical-to-basal dendrite ratio, and spine density on basal dendrites (the site of most L4 input to L2/3 pyramidal cells). There was a modest difference in distribution of apical dendrites, but the functional relevance of this is unclear. Thus high- and low-threshold cells did not map onto L2 vs. L3 morphological types. This is distinct from cortical L5, where burst-generating, thick-tufted pyramidal cells are morphologically distinct from nonbursting, thin-tufted pyramidal cells (Hattox and Nelson 2007; Kasper et al. 1994; Schubert et al. 2006; Seong and Carter 2012). Whether low- and high-threshold cells differ in axonal morphology or targeting remains unknown but is possible, given the recent finding that intrinsic excitability differs between L2/3 pyramidal cells with different long-distance projection targets (Yamashita et al. 2013).

Relationship to fosGFP+ and fosGFP− cells in young mice. In fosGFP transgenic mice, fosGFP+ cells are more spontaneously active than fosGFP− cells in vivo (Yassin et al. 2010), have larger L4-evoked excitatory postsynaptic currents (EPSCs), and have lower L4-evoked spike thresholds (Benedetti et al. 2013). These characteristics are similar to our low-threshold cells. fosGFP+ cells also have reduced intrinsic excitability as revealed by reduced *F-I* slope (Yassin et al. 2010), although the mechanism is distinct from our low-threshold cells (lower R_{input}, higher rheobase, and no difference in spike threshold) (Yassin et al. 2010). Thus our low- and high-threshold cells are likely to overlap substantially with fosGFP+ and fosGFP− cells, respectively.

Our results extend the fosGFP findings in several important ways. First, we show that L2/3 pyramidal cells exhibit a similar gradient of responsiveness across different feedforward synaptic pathways, and that neurons that are more responsive to feedforward (L4 and L5a) input are also more responsive to PW input in vivo. This provides strong evidence that L2/3 pyramidal cells differ in inherent feedforward responsiveness, in addition to any differences in sensory tuning, and that this heterogeneity of responsiveness contributes to the nonuniform distribution of response probability across L2/3 pyramidal cells in vivo. Second, by recording in a relatively unbiased manner from many L2/3 neurons, we conclude that the distribution of feedforward responsiveness appears as a broad gradient, rather than distinct cell subclasses of more and less responsive neurons. This was not clear from binary comparisons of fosGFP+ and fosGFP− neurons. Third, cellular and circuit specializations of fosGFP+ neurons were characterized only in young mice (P12–P15), when L4-L2/3 circuits are immature (Yassin et al. 2010). Our results demonstrate that these specializations persist in older animals (P18–P22), and that response heterogeneity occurs in vivo in adult animals (P30–P45).

Conclusions. We observed a functional gradient of feedforward responsiveness among L2/3 pyramidal cells, which was correlated with gradients of several physiological properties. We failed to detect significant clustering of any physiological property across neurons. This suggests that while more and less responsive neurons exist in L2/3 (represented in part by fosGFP+ and fosGFP− neurons), these represent the tails of a broad functional distribution rather than a small number of discrete pyramidal cell classes. Because subsets of L2/3 pyramidal cells project to different cortical targets (Sato and Svoboda 2010), this suggests that the broad functional distribution of physiological properties in L2/3 is built of multiple subgroups of L2/3 pyramidal cells with overlapping cell physiological properties. In vivo, heterogeneity in response strength among L2/3 neurons is stable over a week or more, suggesting that it is an essential framework for sensory coding (Margolis et al. 2012). It may also critically guide plasticity (Margolis et al. 2012), which may be distinct in high- and low-responsive neurons (Hardingham et al. 2011; Holtmaat et al. 2006; Jacob et al. 2012).

ACKNOWLEDGMENTS

We thank Dhruba Banerjee, Justin Choi, and Sofia Essayan-Perez for histology and morphological analysis.

Present address of J. Elstrott: Genentech, mail stop 228, 1 DNA Way, South San Francisco, CA 94080.

GRANTS

This work was supported by National Institute of Neurological Disorders and Stroke (NINDS) Grant R01 NS-072416 and by NINDS Grant F32 NS-073279 to J. Elstrott.

DISCLOSURES

No conflicts of interest, financial or otherwise, are declared by the author(s).

AUTHOR CONTRIBUTIONS

Author contributions: J.E. and D.E.F. conception and design of research; J.E., K.C., H.J., and I.A. performed experiments; J.E., K.C., H.J., and I.A. analyzed data; J.E., K.C., and D.E.F. interpreted results of experiments; J.E. and K.C. prepared figures; J.E. drafted manuscript; J.E. and D.E.F. edited and revised manuscript; J.E. and D.E.F. approved final version of manuscript.

REFERENCES

Abràmoff MD, Magalhães PJ, Ram SJ. Image processing with ImageJ. *Biophotonics Int* 11: 36–42, 2004.

Agmon A, Connors BW. Thalamocortical responses of mouse somatosensory (barrel) cortex in vitro. *Neuroscience* 41: 365–379, 1991.

Andermann ML, Moore CI. A somatotopic map of vibrissa motion direction within a barrel column. *Nat Neurosci* 9: 543–551, 2006.

Barlow HB. Single units and sensation: a neuron doctrine for perceptual psychology? *Perception* 1: 371–394, 1972.

Barth AL, Gerkin RC, Dean KL. Alteration of neuronal firing properties after in vivo experience in a FosGFP transgenic mouse. *J Neurosci* 24: 6466–6475, 2004.

Barth AL, Poulet JF. Experimental evidence for sparse firing in the neocortex. *Trends Neurosci* 35: 345–355, 2012.

Bender KJ, Rangel J, Feldman DE. Development of columnar topography in the excitatory layer 4 to layer 2/3 projection in rat barrel cortex. *J Neurosci* 23: 8759–8770, 2003.

Benedetti BL, Takashima Y, Wen JA, Urban-Ciecko J, Barth AL. Differential wiring of layer 2/3 neurons drives sparse and reliable firing during neocortical development. *Cereb Cortex* 23: 2690–2699, 2013.

Bureau I, Von Saint Paul F, Svoboda K. Interdigitated paralemniscal and lemniscal pathways in the mouse barrel cortex. *PLoS Biol* 4: e382, 2006.

Bureau I, Shepherd GM, Svoboda K. Precise development of functional and anatomical columns in the neocortex. *Neuron* 42: 789–801, 2004.

Connors BW, Gutnick MJ. Intrinsic firing patterns of diverse neocortical neurons. *Trends Neurosci* 13: 99–104, 1990.

Crochet S, Poulet JF, Kremer Y, Petersen CC. Synaptic mechanisms underlying sparse coding of active touch. *Neuron* 69: 1160–1175, 2011.

de Kock CP, Bruno RM, Spors H, Sakmann B. Layer- and cell-type-specific suprathreshold stimulus representation in rat primary somatosensory cortex. *J Physiol* 581: 139–154, 2007.

de Kock CP, Sakmann B. Spiking in primary somatosensory cortex during natural whisking in awake head-restrained rats is cell-type specific. *Proc Natl Acad Sci USA* 106: 16446–16450, 2009.

Defelipe J, López-Cruz PL, Benavides-Piccione R, Bielza C, Larrañaga P, Anderson S, Burkhalter A, Cauli B, Fairén A, Feldmeyer D, Fishell G, Fitzpatrick D, Freund TF, González-Burgos G, Hestrin S, Hill S, Hof PR, Huang J, Jones EG, Kawaguchi Y, Kisvárday Z, Kubota Y, Lewis DA, Marin O, Markram H, McBain CJ, Meyer HS, Monyer H, Nelson SB, Rockland K, Rossier J, Rubenstein JL, Rudy B, Scanziani M, Shepherd GM, Sherwood CC, Staiger JF, Tamás G, Thomson A, Wang Y, Yuste R, Ascoli GA. New insights into the classification and nomenclature of cortical GABAergic interneurons. *Nat Rev Neurosci* 14: 202–216, 2013.

Desai NS, Rutherford LC, Turrigiano GG. Plasticity in the intrinsic excitability of cortical pyramidal neurons. *Nat Neurosci* 2: 515–520, 1999.

Drew PJ, Feldman DE. Intrinsic signal imaging of deprivation-induced contraction of whisker representations in rat somatosensory cortex. *Cereb Cortex* 19: 331–348, 2009.

Estebanez L, El Boustani S, Destexhe A, Shulz DE. Correlated input reveals coexisting coding schemes in a sensory cortex. *Nat Neurosci* 15: 1691–1699, 2012.

Feldmeyer D, Brecht M, Helmchen F, Petersen CC, Poulet JF, Staiger JF, Luhmann HJ, Schwarz C. Barrel cortex function. *Prog Neurobiol* 103: 3–27, 2013.

Feldmeyer D, Lübke J, Sakman B. Efficacy and connectivity of intracolumnar pairs of layer 2/3 pyramidal cells in the barrel cortex of juvenile rats. *J Physiol* 575: 583–602, 2006.

Feldmeyer D, Lübke J, Silver RA, Sakmann B. Synaptic connections between layer 4 spiny neurone-layer 2/3 pyramidal cell pairs in juvenile rat barrel cortex: physiology and anatomy of interlaminar signalling within a cortical column. *J Physiol* 538: 803–822, 2002.

Golowasch J, Thomas G, Taylor AL, Patel A, Pineda A, Khalil C, Nadim F. Membrane capacitance measurements revisited: dependence of capacitance value on measurement method in nonisopotential neurons. *J Neurophysiol* 102: 2161–2175, 2009.

Graves AR, Moore SJ, Bloss EB, Mensh BD, Kath WL, Spruston N. Hippocampal pyramidal neurons comprise two distinct cell types that are countermodulated by metabotropic receptors. *Neuron* 76: 776–789, 2012.

Hardingham NR, Gould T, Fox K. Anatomical and sensory experiential determinants of synaptic plasticity in layer 2/3 pyramidal neurons of mouse barrel cortex. *J Comp Neurol* 519: 2090–2124, 2011.

Hattox AM, Nelson SB. Layer V neurons in mouse cortex projecting to different targets have distinct physiological properties. *J Neurophysiol* 98: 3330–3340, 2007.

Holtmaat A, Wilbrecht L, Knott GW, Welker E, Svoboda K. Experience-dependent and cell-type-specific spine growth in the neocortex. *Nature* 441: 979–983, 2006.

House DR, Elstrott J, Koh E, Chung J, Feldman DE. Parallel regulation of feedforward inhibition and excitation during whisker map plasticity. *Neuron* 72: 819–831, 2011.

Jacob V, Petreanu L, Wright N, Svoboda K, Fox K. Regular spiking and intrinsic bursting pyramidal cells show orthogonal forms of experience-dependent plasticity in layer V of barrel cortex. *Neuron* 73: 391–404, 2012.

Jadhav SP, Wolfe J, Feldman DE. Sparse temporal coding of elementary tactile features during active whisker sensation. *Nat Neurosci* 12: 792–800, 2009.

Kapfer C, Glickfeld LL, Atallah BV, Scanziani M. Supralinear increase of recurrent inhibition during sparse activity in the somatosensory cortex. *Nat Neurosci* 10: 743–753, 2007.

Kasper EM, Larkman AU, Lübke J, Blakemore C. Pyramidal neurons in layer 5 of the rat visual cortex. I. Correlation among cell morphology, intrinsic electrophysiological properties, and axon targets. *J Comp Neurol* 339: 459–474, 1994.

Kerr JN, de Kock CP, Greenberg DS, Bruno RM, Sakmann B, Helmchen F. Spatial organization of neuronal population responses in layer 2/3 of rat barrel cortex. *J Neurosci* 27: 13316–13328, 2007.

Lambo ME, Turrigiano GG. Synaptic and intrinsic homeostatic mechanisms cooperate to increase L2/3 pyramidal neuron excitability during a late phase of critical period plasticity. *J Neurosci* 33: 8810–8819, 2013.

Larkum ME, Waters J, Sakmann B, Helmchen F. Dendritic spikes in apical dendrites of neocortical layer 2/3 pyramidal neurons. *J Neurosci* 27: 8999–9008, 2007.

Lübke J, Roth A, Feldmeyer D, Sakmann B. Morphometric analysis of the columnar innervation domain of neurons connecting layer 4 and layer 2/3 of juvenile rat barrel cortex. *Cereb Cortex* 13: 1051–1063, 2003.

Margolis DJ, Lütcke H, Schulz K, Haiss F, Weber B, Kügler S, Hasan MT, Helmchen F. Reorganization of cortical population activity imaged throughout long-term sensory deprivation. *Nat Neurosci* 15: 1539–1546, 2012.

Meyer HS, Schwarz D, Wimmer VC, Schmitt AC, Kerr JN, Sakmann B, Helmstaedter M. Inhibitory interneurons in a cortical column form hot zones of inhibition in layers 2 and 5A. *Proc Natl Acad Sci USA* 108: 16807–16812, 2011.

Meyer HS, Wimmer VC, Oberlaender M, de Kock CP, Sakmann B, Helmstaedter M. Number and laminar distribution of neurons in a thalamocortical projection column of rat vibrissal cortex. *Cereb Cortex* 20: 2277–2286, 2010.

Moore CI, Nelson SB. Spatio-temporal subthreshold receptive fields in the vibrissa representation of rat primary somatosensory cortex. *J Neurophysiol* 80: 2882–2892, 1998.

O'Connor DH, Clack NG, Huber D, Komiyama T, Myers EW, Svoboda K. Vibrissa-based object localization in head-fixed mice. *J Neurosci* 30: 1947–1967, 2010a.

O'Connor DH, Peron SP, Huber D, Svoboda K. Neural activity in barrel cortex underlying vibrissa-based object localization in mice. *Neuron* 67: 1048–1061, 2010b.

Oberlaender M, de Kock CP, Bruno RM, Ramirez A, Meyer HS, Dercksen VJ, Helmstaedter M, Sakmann B. Cell type-specific three-dimensional structure of thalamocortical circuits in a column of rat vibrissal cortex. *Cereb Cortex* 22: 2375–2391, 2012.

Olshausen BA, Field DJ. Sparse coding of sensory inputs. *Curr Opin Neurobiol* 14: 481–487, 2004.

Perkins KL. Cell-attached voltage-clamp and current-clamp recording and stimulation techniques in brain slices. *J Neurosci Methods* 154: 1–18, 2006.

Petersen CC, Sakmann B. The excitatory neuronal network of rat layer 4 barrel cortex. *J Neurosci* 20: 7579–7586, 2000.

Pologruto TA, Sabatini BL, Svoboda K. ScanImage: flexible software for operating laser scanning microscopes. *Biomed Eng Online* 2: 13, 2003.

Porter JT, Johnson CK, Agmon A. Diverse types of interneurons generate thalamus-evoked feedforward inhibition in the mouse barrel cortex. *J Neurosci* 21: 2699–2710, 2001.

Pouille F, Marin-Burgin A, Adesnik H, Atallah BV, Scanziani M. Input normalization by global feedforward inhibition expands cortical dynamic range. *Nat Neurosci* 12: 1577–1585, 2009.

Sarid L, Feldmeyer D, Gidon A, Sakmann B, Segev I. Contribution of intracolumnar layer 2/3-to-layer 2/3 excitatory connections in shaping the response to whisker deflection in rat barrel cortex. *Cereb Cortex* (October 27, 2013). doi:10.1093/cercor/bht268.

Sasaki T, Takahashi N, Matsuki N, Ikegaya Y. Fast and accurate detection of action potentials from somatic calcium fluctuations. *J Neurophysiol* 100: 1668–1676, 2008.

Sato TR, Gray NW, Mainen ZF, Svoboda K. The functional microarchitecture of the mouse barrel cortex. *PLoS Biol* 5: e189, 2007.

Sato TR, Svoboda K. The functional properties of barrel cortex neurons projecting to the primary motor cortex. *J Neurosci* 30: 4256–4260, 2010.

Schubert D, Kotter R, Luhmann HJ, Staiger JF. Morphology, electrophysiology and functional input connectivity of pyramidal neurons characterizes a genuine layer Va in the primary somatosensory cortex. *Cereb Cortex* 16: 223–236, 2006.

Seong HJ, Carter AG. D1 receptor modulation of action potential firing in a subpopulation of layer 5 pyramidal neurons in the prefrontal cortex. *J Neurosci* 32: 10516–10521, 2012.

Shao YR, Isett BR, Miyashita T, Chung J, Pourzia O, Gasperini RJ, Feldman DE. Plasticity of recurrent L2/3 inhibition and gamma oscillations by whisker experience. *Neuron* 80: 210–222, 2013.

Shepherd GM, Stepanyants A, Bureau I, Chklovskii D, Svoboda K. Geometric and functional organization of cortical circuits. *Nat Neurosci* 8: 782–790, 2005.

Shepherd GM, Svoboda K. Laminar and columnar organization of ascending excitatory projections to layer 2/3 pyramidal neurons in rat barrel cortex. *J Neurosci* 25: 5670–5679, 2005.

Silberberg G, Markram H. Disynaptic inhibition between neocortical pyramidal cells mediated by Martinotti cells. *Neuron* 53: 735–746, 2007.

Stosiek C, Garaschuk O, Holthoff K, Konnerth A. In vivo two-photon calcium imaging of neuronal networks. *Proc Natl Acad Sci USA* 100: 7319–7324, 2003.

Thévenaz PP, Ruttimann UE, Unser MM. A pyramid approach to subpixel registration based on intensity. *IEEE Trans Image Process* 7: 27–41, 1998.

Vogelstein J, Packer AM, Machado TA, Sippy T, Babadi B, Yuste R, Paninski L. Fast nonnegative deconvolution for spike train inference from population calcium imaging. *J Neurophysiol* 104: 3691–3704, 2010.

Wehr M, Zador AM. Balanced inhibition underlies tuning and sharpens spike timing in auditory cortex. *Nature* 426: 442–446, 2003.

Wei W, Elstrott J, Feller MB. Two-photon targeted recording of GFP-expressing neurons for light responses and live-cell imaging in the mouse retina. *Nat Protoc* 5: 1347–1352, 2010.

Wolfe J, Houweling AR, Brecht M. Sparse and powerful cortical spikes. *Curr Opin Neurobiol* 20: 306–312, 2010.

Yamashita T, Pala A, Pedrido L, Kremer Y, Welker E, Petersen CC. Membrane potential dynamics of neocortical projection neurons driving target-specific signals. *Neuron* 80: 1477–1490, 2013.

Yassin L, Benedetti BL, Jouhanneau JS, Wen JA, Poulet JF, Barth AL. An embedded subnetwork of highly active neurons in the neocortex. *Neuron* 68: 1043–1050, 2010.

Zaitsev AV, Povysheva NV, Gonzalez-Burgos G, Lewis DA. Electrophysiological classes of layer 2/3 pyramidal cells in monkey prefrontal cortex. *J Neurophysiol* 108: 595–609, 2012.